Article

Not peer-reviewed version

Analysis of Ionospheric TEC and DCB Using GPS/Galileo Observations from a Moving Training Ship

Byung-Kyu Choi * , Dong-Hyo Sohn , Jong-Kyun Chung , Dong-Jin Han

Posted Date: 25 February 2026

doi: 10.20944/preprints202602.1581.v1

Keywords: GNSS; TEC; correlation coefficient; DCB

Article

Analysis of Ionospheric TEC and DCB Using GPS/Galileo Observations from a Moving Training Ship

Byung-Kyu Choi [1,*], Dong-Hyo Sohn [1], Jong-Kyun Chung [1] and Dong-Jin Han [2]

[1] Korea Astronomy and Space Science Institute, Daejeon 34055, Korea
[2] National Research Foundation, Daejeon 34113, Korea
* Correspondence: bkchoi@kasi.re.kr; Tel.: +82-42-865-3237

Abstract

This study investigates ionospheric total electron content (TEC) and differential code bias (DCB) based on GPS and Galileo data collected aboard the training ship (HANS) from DOY 249 to 300 in 2024. The estimated TEC was compared with the Center for Orbit Determination in Europe (CODE) global ionospheric map (GIM), resulting in a mean difference of –2.41 TEC units (TECU) and a root mean square (RMS) error of 6.53 TECU. Furthermore, although inland GNSS stations in South Korea were incorporated to stabilize receiver DCB estimation, the results still exhibited significant temporal fluctuations. The Pearson correlation revealed a moderate negative relationship between the receiver DCB change and the Dst index, with a correlation coefficient (R) of –0.35. It suggests that geomagnetic disturbances influence receiver DCB changes. The R between receiver DCB and the Kp index was approximately 0.18, while that with the F10.7a index was about –0.26, both indicating a relatively weak correlation. In addition, receiver DCB changes exhibited a positive correlation (R ~ 0.33) with vertical TEC (VTEC). Multipath errors showed negligible correlation with receiver DCB changes. Therefore, we suggest that the significant variability in the receiver DCB on the HANS has a strong correlation with the Dst and VTEC. It can also be attributed to the complex interaction of several factors.

Keywords: GNSS; TEC; correlation coefficient; DCB

---

1. Introduction

The ionosphere is an ionized region of the Earth's upper atmosphere, ranging approximately from 60 km to 1,000 km in altitude. This region significantly impacts the propagation of radio signals used by Global Navigation Satellite Systems (GNSS), including GPS, GLONASS, Galileo, and BeiDou [1–3]. When GNSS signals pass through the ionosphere, they experience group delay and phase advance proportional to the total electron content (TEC) along their paths. Accurate estimation of TEC is therefore essential for correcting ionospheric delay errors in GNSS positioning, especially in high-precision applications such as geodesy, navigation, and remote sensing [4–7].

The use of shipborne GNSS offers several advantages. Ships can travel across vast oceanic areas, enabling the collection of spatially distributed data that complements land-based measurements. This is especially beneficial for monitoring Precipitable Water Vapor (PWV) and TEC. Several studies have demonstrated the feasibility and utility of shipborne GNSS for PWV estimation [8–10]. Wang et al. [8] deployed GNSS receivers on research vessels traversing the western Pacific Ocean and compared GNSS-derived PWV with data from radiosondes and reanalysis. Their results showed a high correlation between GNSS PWV and radiosonde, with mean absolute differences typically below 2 mm. Therefore, they validated the reliability of GNSS PWV retrievals at sea. Sohn et al. [11] also reported that shipborne GNSS-derived PWV shows good agreement with PWV retrieved from radiosonde measurements.

One of the key parameters used to characterize ionospheric effects on GNSS signals is the TEC. Ground-based GNSS stations have been widely used to estimate ionospheric TEC over land [12–16]. However, due to the limited availability of observational infrastructure over the oceans, accurately estimating TEC in these regions remains a significant challenge. Despite the increasing number of GNSS satellites, the lack of observations over the oceans remains a significant limitation. In particular, insufficient GNSS infrastructure has emerged as a major constraint in equatorial and mid-latitude oceanic regions where ionospheric variability is often pronounced. To overcome these observational limitations, the deployment of GNSS instruments on mobile marine platforms, such as research vessels, commercial ships, and ocean buoys, has emerged as an alternative. The shipborne GNSS receivers can collect GNSS data across vast oceanic areas. They can also contribute to a more comprehensive understanding of ionospheric TEC monitoring over the seas. A study analyzed the characteristics of the Equatorial Ionization Anomaly (EIA) using shipborne GNSS data [16]. Wang et al. [17] estimated ionospheric TEC within the Arctic Circle using GPS data collected from a ship. They reported that the difference between the global ionospheric model TEC and the actual ionospheric TEC in the Arctic Circle region is approximately 3 to 6 TEC Units (TECU).

To overcome this limitation in the ocean, a variety of spaceborne and ocean-based platforms have been employed to extend ionospheric TEC monitoring [18]. Several satellite missions have contributed to ionospheric TEC or electron density profile (EDP) measurements, including TOPEX/Poseidon [19], the Constellation Observing System for Meteorology, Ionosphere, and Climate (COSMIC) [20,21], and the COSMIC-2 mission [22]. It is noteworthy that satellite altimetry missions such as TOPEX/Poseidon, Jason-1, Jason-2, Jason-3, and Sentinel-6 have provided valuable dual-frequency measurements that can be used to estimate ionospheric TEC over the oceans. These missions are originally designed for sea surface height and ocean circulation studies. They transmit radar pulses at two frequencies of Ku and C band or Ku and S band for the estimation of vertically integrated electron content above the satellite's field of view.

Research on ionospheric TEC using GPS/Galileo observations on the ship remains relatively underexplored. This study investigates the accuracy of ionospheric TEC and differential code bias (DCB) correlations with some factors using GNSS equipment deployed on the training ship (HANS). We also compare our results with the Center for Orbit Determination in Europe (CODE) global ionospheric maps (GIM) TEC.

2. GNSS Experimental Environment and Description of the HANS

2.1. Description of the HANS

For the purpose of investigating ionospheric TEC over oceanic regions, the GNSS equipment was deployed on the HANS, which is operated by the Republic of Korea (ROK) Navy. The HANS is an auxiliary training ship of the ROK Navy, purpose-built to fulfill educational, logistical, and support roles. This ship was constructed by Hyundai Heavy Industries, which is one of the leading shipbuilders (https://www.navalnews.com/naval-news/2020/10/rok-navy-took-delivery-of-first-ever-dedicated-training-ship/?utm_source). It was officially commissioned in April 2021. Designed with operational versatility and extended sea endurance in mind, the vessel features a standard displacement of approximately 4,500 tons, increasing to 6,000 tons when fully loaded. It has a total length of 142 meters, a beam of 25 meters, which enables it to maintain stability in various sea states (https://en.wikipedia.org/wiki/ROKS_Hansando?utm_source).

Figure 1 illustrates the installation location and physical configuration of the GNSS antenna on the *HANS. As shown in Figure 1,* an upper right box zooms into the actual installed GNSS antenna, mounted on the port side of the bridge's upper platform railing. The antenna model equipped on the ship is a PolaNt-x MF.v2, which is capable of a high-precision, multi-frequency, and multi-constellation design for advanced positioning and navigation applications. In addition, this antenna is complemented by a PolaRx5 GNSS receiver from Septentrio Co., which enables precise and reliable positioning through support for multiple satellite constellations.

Figure 1. The installation location and physical configuration of the GNSS Antenna on the HANS (https://bemil.chosun.com/nbrd/bbs/view.html?b_bbs_id=10158&pn=1&num=5439).

2.2. GNSS Experimental Environment

The HANS conducted a 52-day operation in the North Pacific Ocean from Day of Year (DOY) 249 to 300 in 2024. Figure 2 shows the route trajectory of the HANS for 52 days, as well as the locations of static GNSS stations used in this study. The ship exhibits diverse movement patterns, extending from approximately 50^0 N to areas close to the equatorial regions. As shown in Figure 2, the red dots mark the positions of the inland GNSS sites, which are located in South Korea. The blue dotted line represents the route trajectory of the HANS.

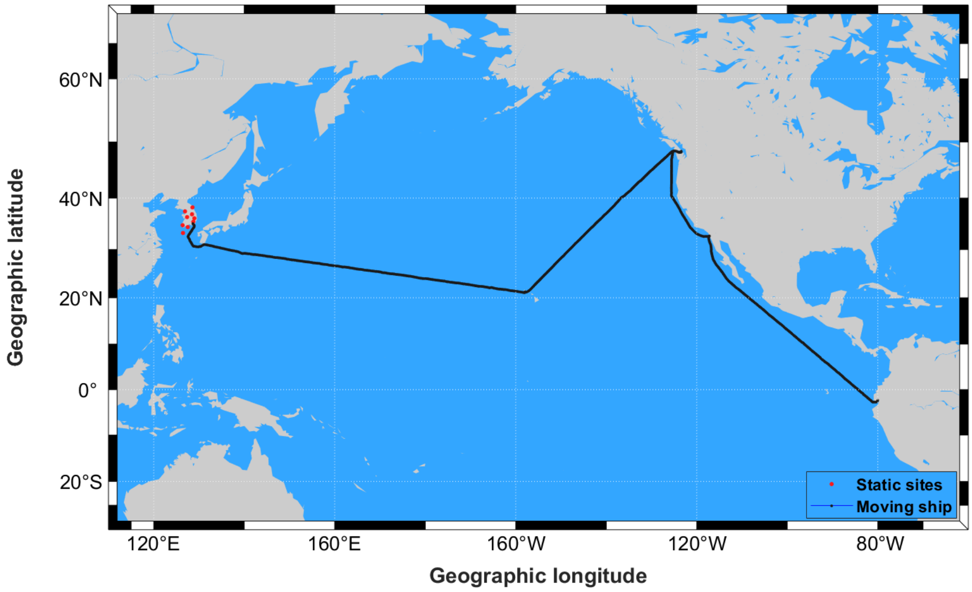

Figure 2. The route trajectory of the HANS. The positions of the static GNSS sites are marked as red dots. The blue dot line denotes the ship's motions.

Table 1 presents the models of GNSS receivers and antennas used at the stations and on the HANS for data processing. The GNSS stations (skch, skma, sbao, daej, bhao, mlyn, mkpo, and jeju) in the inland are equipped with the Trimble NetR9 receiver paired with a TRM59800.00 SCIS antenna. The TRM59800.00 SCIS antenna is designed as a choke ring type. The kohg GNSS station utilizes the latest Trimble Alloy receiver paired with the same antenna model (TRM59800.00 SCIS), ensuring consistency across the network while improving signal processing capabilities.

The kinematic mode of the ship refers to a GNSS positioning configuration in which the receiver is installed on a moving platform and collects continuous positioning results. In static mode, the receiver positions remain fixed at the known value, whereas in the kinematic mode, the moving ship's position has to be calculated continuously.

The GNSS data received from the receiver on the HANS is logged in real time. We process the GNSS data into the Receiver Independent Exchange Format (RINEX) version 3.0 format, which has an interval of 30 seconds.

Table 1. The receiver and antenna equipment on the inland GNSS stations and HANS.

Site name	Receiver type	Antenna type	Position mode
skch	TRIMBLE NetR9	TRM59800.00 SCIS	Static
skma	TRIMBLE NetR9	TRM59800.00 SCIS	Static
sbao	TRIMBLE NetR9	TRM59800.00 SCIS	Static
daej	TRIMBLE NetR9	TRM59800.00 SCIS	Static
bhao	TRIMBLE NetR9	TRM59800.00 SCIS	Static
mlyn	TRIMBLE NetR9	TRM59800.00 SCIS	Static
mkpo	TRIMBLE NetR9	TRM59800.00 SCIS	Static
kohg	TRIMBLE Alloy	TRM59800.00 SCIS	Static
jeju	TRIMBLE NetR9	TRM59800.00 SCIS	Static
HANS	SEPT PolaRx5	PolaNt-x MF.v2	Kinematic

3. TEC Estimation Method

Accurate estimation of ionospheric TEC using only a single GNSS station remains a significant challenge. The limited number of observations can severely degrade the accuracy of TEC and DCB estimations in TEC modeling [23,24]. It is common to estimate ionospheric TEC using a GNSS network with high spatial resolution. Such dense networks provide improved observational geometry, enabling more accurate characterization of ionospheric structures and their temporal variations.

In this study, ionospheric TEC is estimated using dual-frequency GPS/Galileo observations obtained from a GNSS receiver installed on the *HANS*. In particular, estimating TEC from a moving ship is notably difficult. Therefore, additional data from GNSS stations on the Korean Peninsula can be utilized to enhance the robustness of the TEC estimation due to the inherent instability in estimating DCBs from shipborne platforms.

Some studies have utilized both GPS and Galileo constellation for ionospheric TEC estimation [25,26]. GPS primarily provides observations on the L1 (1575.42 MHz) and L2 (1227.60 MHz) frequencies, whereas Galileo offers signals on the E1 (1575.42 MHz) and E5a (1176.45 MHz)

Preprints.org (www.preprints.org) | NOT PEER-REVIEWED | Posted: 25 February 2026 doi:10.20944/preprints202602.1581.v1

frequencies. Therefore, we considered TEC estimation using different frequency combinations as follows [26]:

$$TEC_{GPS} = \frac{f_1^2 \cdot f_2^2}{K \cdot (f_1^2 - f_2^2)} \cdot [(L1 - L2) - DCB_{12}] \quad (1)$$

$$TEC_{Galileo} = \frac{f_1^2 \cdot f_5^2}{K \cdot (f_1^2 - f_5^2)} \cdot [(E1 - E5a) - DCB_{15}] \quad (2)$$

Where the constant K is 40.3 m^3/s^2, which is a physical constant related to ionospheric refraction. f_1, f_2, and f_5 denote the carrier frequencies of the L1 (E1), L2, and E5a signals. DCB represents the time delay differences between code signals of different frequencies caused by satellite and receiver hardware.

DCB is one of the most significant error sources in the estimation of ionospheric TEC [27–32]. In this study, we employ a spherical harmonic expansion method and a least squares approach to obtain DCB values for the GPS/Galileo receiver and satellite. While simultaneous estimation of TEC and DCB is generally feasible in environments with dense and continuous GNSS observations, the dynamic nature of a moving ship and the limited data availability may require a sequential approach. In this study, DCB values are first estimated and then subsequently applied to the TEC calculation. Furthermore, since DCBs exist in both the receivers and the satellites, it is essential to separate them accurately [33–36]. To separate the receiver and satellite DCBs, we apply the constraint that the sum of satellite DCBs equals zero.

Accurate estimation of both satellite and receiver DCBs from observations of a single GNSS receiver onboard a ship remains a significant challenge due to the limited spatial and temporal diversity of the data. Given that DCBs are a major source of error in the retrieval of ionospheric TEC, this study adopts a hybrid approach that incorporates observations from inland stations in South Korea to enhance the stability of DCB estimation. Initially, combined measurements from the shipborne receiver and inland GNSS stations are utilized to estimate the GPS/Galileo DCBs of both satellites and receivers simultaneously. The estimated DCBs are then applied to dual-frequency GPS and Galileo observations to compute ionospheric TEC.

Figure 3 illustrates the processing flow for calculating ionospheric TEC from the continuously moving HANS ship. For IPP calculation, the fixed positions of inland stations are obtained directly from RINEX observation files, whereas the positions of the HANS are computed at each epoch using dual-frequency code observables and broadcast ephemerides. GPS/Galileo receiver and satellite DCBs are estimated using data obtained from the inland GNSS station and the HANS ship. The DCB values are generated on a daily basis. Therefore, the ionospheric TEC from the HANS is estimated with the GPS/Galileo observations using the precomputed daily DCB values.

doi:10.20944/preprints202602.1581.v1

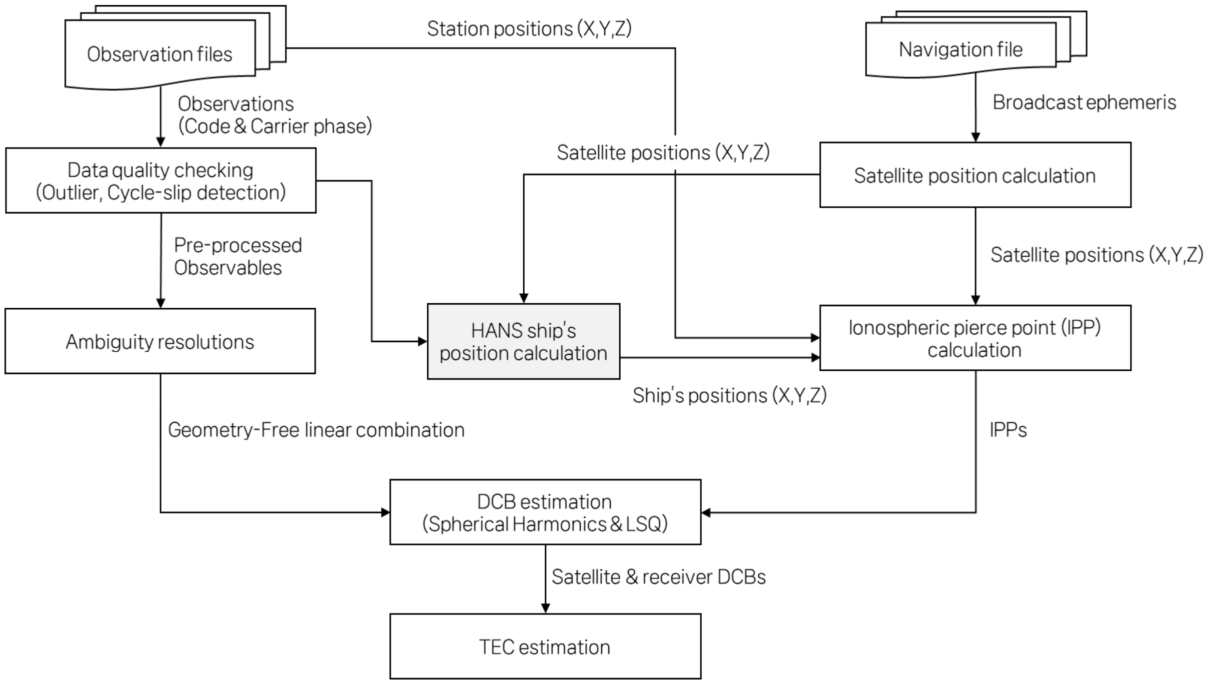

Figure 3. The flow chart for ionospheric TEC estimation.

4. Results

4.1. IPPs from the HANS

In ionospheric TEC modeling, the assumption of a fixed ionospheric shell height plays a critical role in determining the location of the Ionospheric Pierce Point (IPP), which refers to the specific point at which a GNSS signal penetrates the ionosphere. In general, a single-layer model as a thin shell is adopted for ionospheric TEC modeling [37–41]. The altitude of the thin shell is assumed to be around 350 to 450 km above the Earth's surface. In this study, we assumed the fixed altitude to be 350 km.

The HANS traveled from the southern coast of the Korean Peninsula to Ecuador in South America between DOY 249 and 300 in 2024. Figure 4 shows the spatial distribution of IPPs and the corresponding vertical TEC (VTEC) values along the trajectory of the HANS. The black line represents the actual route of the ship, while the colored lines extending from this trajectory indicate the IPPs derived from GPS and Galileo satellites. The VTEC values are color-coded according to the vertical bar on the right, ranging from 0 to 150 TECU. Blue to green colors denote relatively low TEC regions, whereas yellow to red shades represent areas with elevated ionospheric activity. Relatively large VTEC values are observed near the equatorial region, consistent with the EIA. Conversely, low VTEC values appear at higher latitudes.

Figure 4a-b also shows the temporal and spatial variations in ionospheric electron content over the Pacific Ocean and across equatorial and mid-latitude regions, providing insight into the benefits of shipborne GPS/Galileo measurements for ionospheric TEC monitoring in under-sampled oceanic areas. It can be seen that the GPS IPP distribution is very similar to that of Galileo.

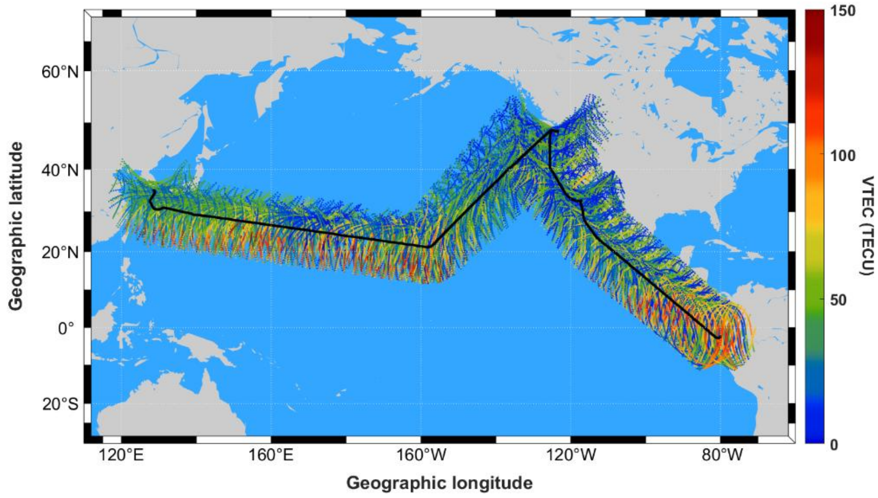

(a) GPS IPPs and VTEC values

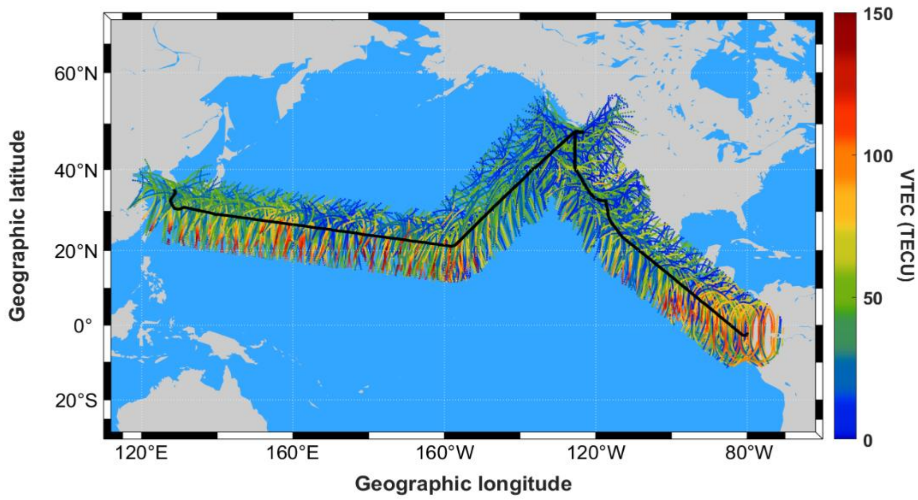

(b) Galileo IPPs and VTEC values

Figure 4. IPP distribution and VTEC values along the HANS's route. The black line represents the HANS's route during the period of DOY 249 to 294, 2024. The colored lines indicate the IPPs and VTEC values derived from (a) GPS and (b) Galileo satellites.

4.2. DCB Analysis

Ionospheric TEC can be estimated using GNSS signals transmitted at different frequencies. To retrieve TEC, the geometry-free linear combination of dual-frequency GNSS code observations is commonly employed. However, each GNSS signal inherently includes frequency-dependent hardware biases, which are also differenced in the geometry-free combination. These residual biases are referred to as DCBs [42–47].

Figure 5 presents the time series of satellite DCBs for both the GPS and Galileo. The DCB values were computed daily over the period from DOY 249 to 300 in 2024. For GPS, the C1C and C2W observations were used, while for Galileo, the C1X and C5X observations were utilized. Figure 5a presents the GPS C1C-C2W satellite DCB values estimated in this study. The C1C-C2W DCB values for GPS generally vary within a range of approximately –10 ns to 10 ns. Furthermore, except for a few anomalous days, the satellite DCB estimates exhibit overall temporal stability, suggesting reliable estimation over this period.

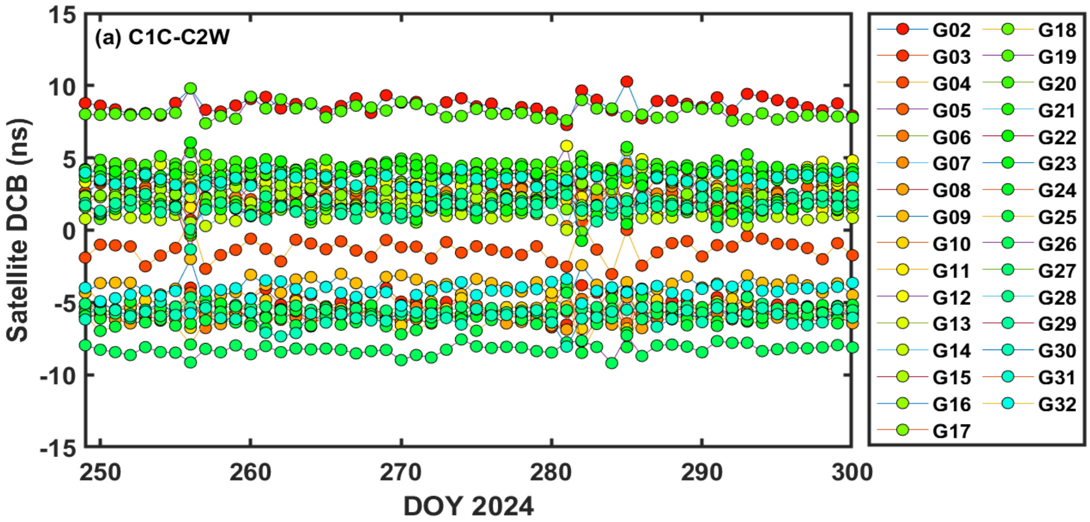

(**a**) GPS satellite C1C-C2W DCB values

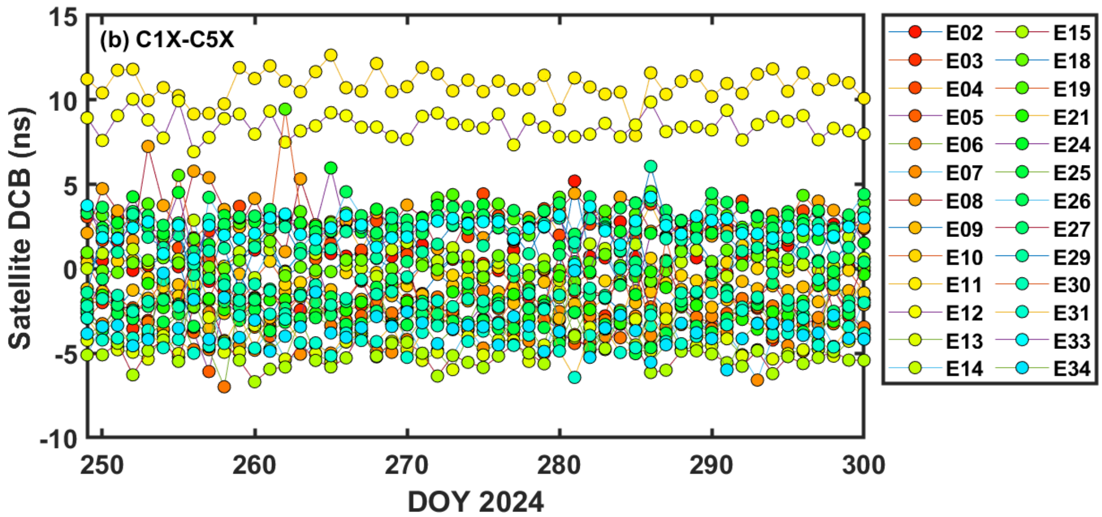

(**b**) Galileo satellite C1X-C5X DCB values

Figure 5. The time series of satellites DCBs from DOY 249 to 300, 2024. (a) GPS satellite C1C-C2W DCBs, (b) Galileo satellite C1X-C5X DCBs.

Figure 5b shows the time series of C1X-C5X satellite DCBs for Galileo. The DCB estimates for Galileo vary approximately between –7 ns and 13 ns. Overall, the C1X-C5X DCBs for Galileo exhibit greater variability compared to the C1C-C2W DCBs of GPS satellites, indicating lower temporal stability. This reduced stability may be attributed to the relatively small number of available observations for Galileo satellites. Some studies have reported that the number of observations can significantly influence the accuracy and stability of DCB estimation [45,48].

Figure 6 presents the time series of GPS/Galileo receiver DCB estimates from DOY 249 to 300 in 2024. The receiver DCBs were computed daily using the corresponding satellite signals, specifically C1C-C2W for GPS and C1X-C5X for Galileo. Figure 6a shows the C1C-C2W receiver DCBs for GPS. The receivers at nine GNSS stations (bhao, mkpo, daej, skch, jeju, kohg, mlyn, sbao, and skma) exhibit relatively stable DCB values, ranging approximately from –20 ns to –12 ns. In contrast, the receiver installed on HANS shows a significantly larger variation, with DCB values fluctuating between −5 ns and 10 ns. This indicates that the DCB values for the shipborne receiver are subject to greater uncertainty compared to those of the stationary inland receivers.

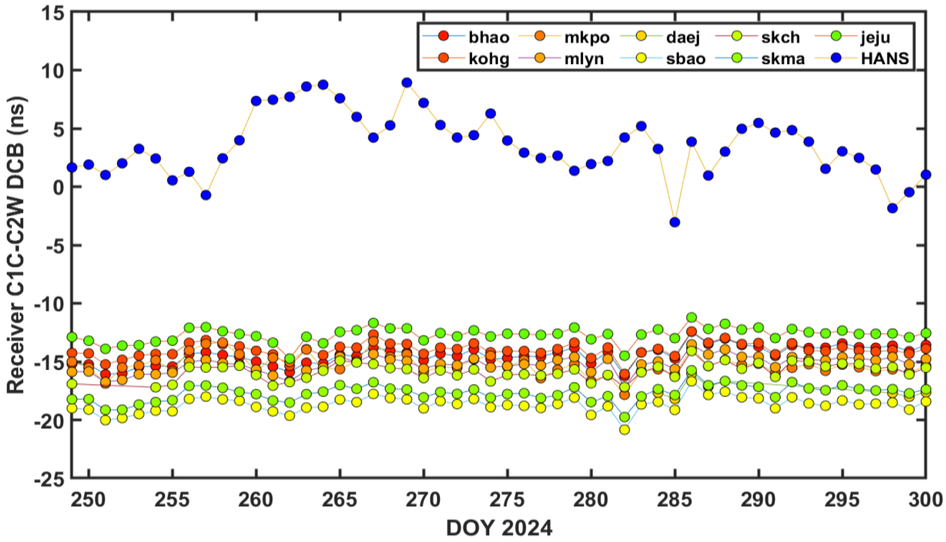

(a) GPS receiver C1C-C2W DCB values

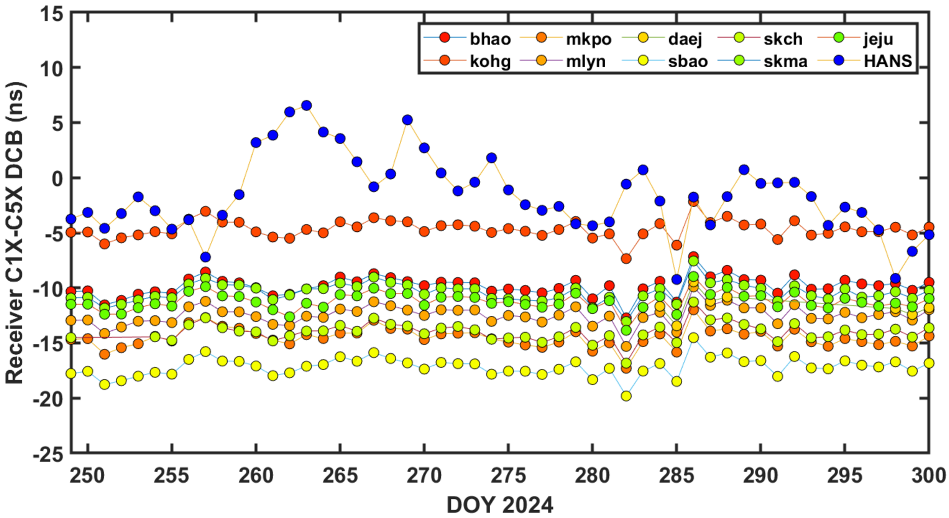

(b) Galileo receiver C1X-C5X DCB values

Figure 6. The time series of the receiver DCBs from DOY 249 to 300, 2024. (a) GPS receiver C1C-C2W DCBs, (b) Galileo receiver C1X-C5X DCBs.

Such instability in the HANS receiver DCB values may be attributed to the dynamic nature of the ship's environment, which introduces increased signal noise, multipath effects, and varying ionospheric conditions along different signal paths. These factors likely contribute to the reduced stability and higher variability observed in the shipborne DCB estimates.

Figure 6b shows the time series of C1X-C5X receiver DCB values for the Galileo. The estimated DCBs range approximately from –20 ns to –3 ns. Similar to the C1C-C2W receiver DCBs, the inland stations showed consistent daily DCB variations. However, the kohg station exhibits different DCB values compared to those of other stations. This discrepancy is attributed to differences in receiver models. Most of the stations employ the Trimble NetR9 receiver model, whereas the kohg station utilizes a Trimble Alloy receiver model.

Furthermore, discrepancies in receiver DCB values are observed even among receivers with the same model. It may be attributed to site-specific environmental conditions, including grounding

doi:10.20944/preprints202602.1581.v1

status and local multipath effects. In addition, the HANS exhibits significantly higher variability in its daily C1X-C5X receiver DCB values. Such instability can be attributed to the dynamic conditions inherent in shipborne GNSS observations, including increased susceptibility to signal degradation, higher noise levels, and limited observational geometry due to the HANS's isolation from dense station networks.

Figure 7 summarizes the results shown in Figure 6 by presenting the mean and root-mean-square (RMS) values of receiver DCBs at each station. Figures 7a and 7b show the mean DCBs and corresponding RMS values in the error bars for C1C-C2W and C1X-C5X DCBs, respectively. While the nine inland stations generally exhibit consistent and low RMS values, the HANS shows significantly larger RMS values for both receiver DCB values. Detailed numerical values for each station are provided in Table 2. Table 2 shows the mean and RMS values of receiver DCBs for both GPS and Galileo at each station. The inland stations display relatively consistent and stable DCB estimates, with RMS values typically below 1.2 ns. In particular, the kohg, jeju, and skch stations showed low RMS values ($\leq$ 0.84 ns), indicating high temporal stability in DCB behavior. Furthermore, the RMS values for the GPS C1C-C2W DCB estimates are consistently lower than those for the Galileo C1X-C5X combination. In contrast, the HANS receiver showed substantially higher RMS values of 2.67 ns and 3.47 ns for the GPS and the Galileo, respectively. This increased instability is likely attributable to the dynamic ship's environment.

It is also noteworthy that the kohg station exhibits a distinguishable offset in its C1X-C5X DCB estimates relative to other stations. Moreover, remarkable differences in DCB values were observed even among the same receiver model. This can be attributed to the specific environmental factors surrounding the receivers [49–52].

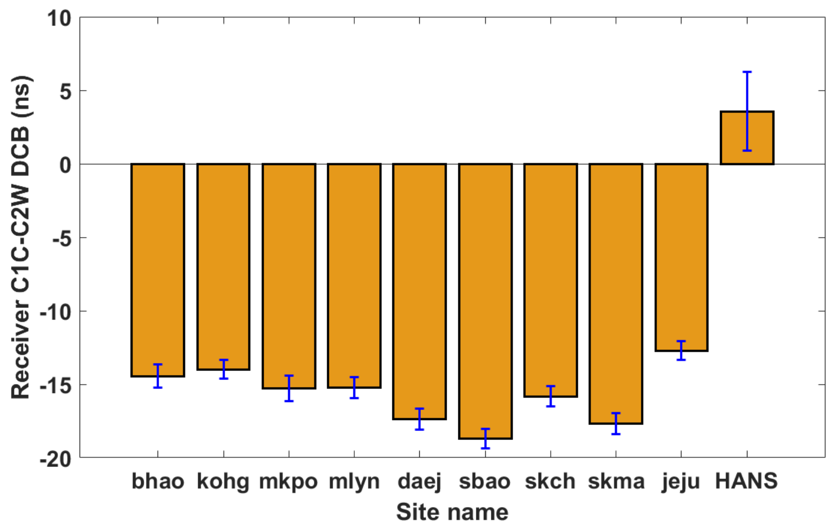

(a) Receiver C1C-C2W DCB values.

doi:10.20944/preprints202602.1581.v1

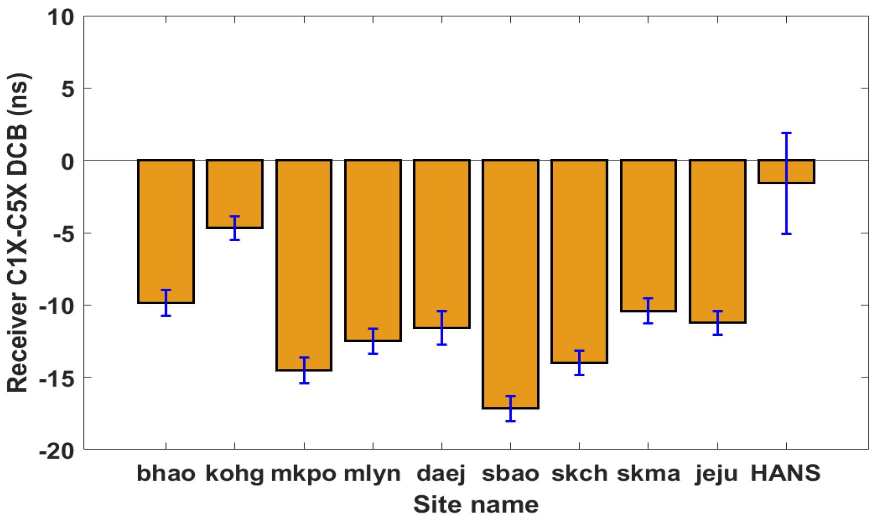

(b) Receiver C1X-C5X DCB values

Figure 7. This is related to Figure 6. The averaged DCB values and RMS values for receivers. (a) Receiver C1C-C2W DCBs, (b) Receiver C1X-C5X DCBs. The yellow bars and blue error bars represent the averaged DCB values and RMS values, respectively.

Table 2. The averaged values and RMS values for the receiver DCBs.

Site name	C1C-C2W DCB (ns)		C1X-C5X DCB (ns)	
	Average	RMS	Average	RMS
bhao	−14.44	0.79	−9.84	0.87
kohg	−13.98	0.63	−4.67	0.81
mkpo	−15.28	0.86	−14.50	0.88
mlyn	−15.23	0.71	−12.47	0.86
daej	−17.37	0.72	−11.58	1.16
sbao	−18.68	0.66	−17.16	0.86
skch	−15.82	0.69	−13.98	0.84
skma	−17.68	0.69	−10.41	0.87
jeju	−12.70	0.64	−11.23	0.80
HANS	3.55	2.67	−1.58	3.49

4.3. TEC Analysis

For comparative analysis of the ionospheric TEC values estimated from the shipborne GPS/Galileo observations, we employed the GIM products provided by the CODE as a reference. Figure 8 shows the time series of VTEC values for the HANS from DOY 249 to 300, 2024. The black line represents the VTEC derived from the GPS/Galileo data collected onboard the HANS, while the red line denotes the corresponding VTEC values obtained from the CODE GIM.

The similar patterns of the two datasets show strong agreement in terms of diurnal variation and magnitude. However, discrepancies between the two datasets were observed intermittently, particularly during specific periods. An average value of the difference between the HANS-derived TEC and the CODE GIM TEC is approximately –2.41 TECU with an RMS of 6.53 TECU. It indicates a reasonable level of consistency between the two sources despite the dynamic environment on the HANS. The substantial fluctuations could largely influence the patterns of overestimation and underestimation observed in the shipborne TEC retrievals in the receiver DCB during this period. In particular, large discrepancies were observed on certain days, particularly from DOY 255 to 270, where the shipborne TEC tends to show higher variability compared to the CODE GIM TEC. These

Preprints.org (www.preprints.org) | NOT PEER-REVIEWED | Posted: 25 February 2026 doi:10.20944/preprints202602.1581.v1

discrepancies can also be attributed to the instability of the HANS's receiver DCB values, as shown in Figure 6.

Nevertheless, the consistency between the HANS-derived TEC and the CODE GIM TEC suggests the possibility of using the shipborne GNSS observations for reliable ionospheric TEC monitoring.

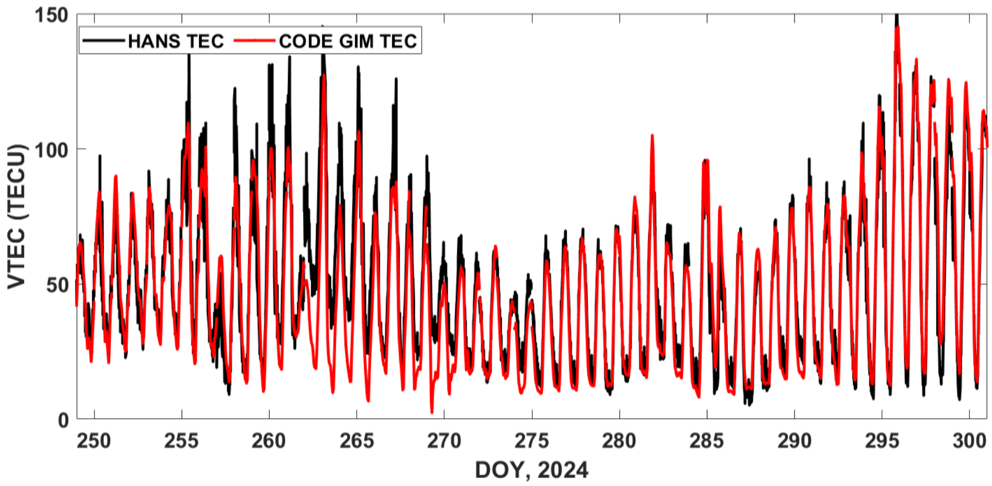

Figure 8. VTEC time series from DOY 249 to 300, 2024. The black and red lines represent the VTEC values for the HANS and the CODE GIM, respectively.

5. Discussion

Discrepancies were observed between the TEC values derived from HANS and those from the CODE GIM. Unlike inland GNSS stations, the receiver DCB values derived from the HANS showed significant variability. Therefore, we investigated a correlation between these differences and variations in several factors.

Figure 9 presents the variations in space weather parameters and geomagnetic indices from DOY 249 to 300, 2024. Figure 9a shows the Disturbance storm time (Dst) value, which is a measure of the global geomagnetic activity. Several geomagnetic storm events were observed during this period. The sharp decrease of the Dst index to below –330 nT on DOY 285 is indicative of an intense geomagnetic storm event. Figure 9b shows the Kp index, a planetary index that quantifies disturbances. The Kp index is reported eight times per day at three-hour intervals. The Kp values exceeding 5 were observed intermittently on DOY 256, 257, 261, 263-265, and during DOY 281-285. These periods are coincident with the sharp decreases in the Dst value, providing further evidence of significant geomagnetic disturbances. Figure 9c presents the F10.7a index, which is the 81-day centered average of the solar radio flux at 10.7 cm (2800 MHz). It is a widely used proxy for solar extreme ultraviolet emissions. The F10.7a values generally range between 150 and 300 solar flux units (sfu) during this period. It reached a value exceeding 300 sfu on DOY 277 and has shown a gradual decreasing trend since then.

doi:10.20944/preprints202602.1581.v1

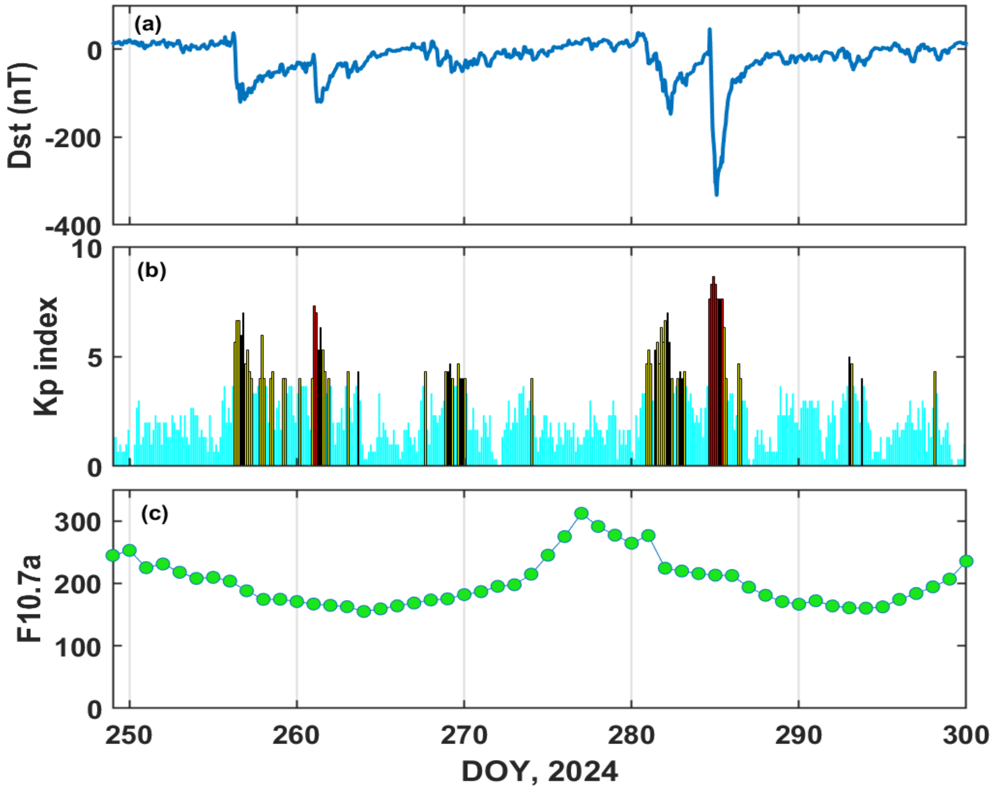

Figure 9. Time series of space weather parameters and geomagnetic indices from DOY 249 to 300, 2024. (a) Dst index, (b) Kp index, and (c) F10.7a index.

We also analyzed the correlations between the receiver DCB values and the three indices presented in Figure 9. Figure 10 shows the correlation coefficients that describe the relationship between the absolute receiver DCB changes and three indices: Dst, Kp, and F10.7a. To show temporal fluctuations in more detail, the receiver DCB change is defined as the absolute deviation of each daily DCB value from the average value over this period. In addition, the Dst and Kp indices were converted to daily averaged values for the correlation analysis.

 doi:10.20944/preprints202602.1581.v1

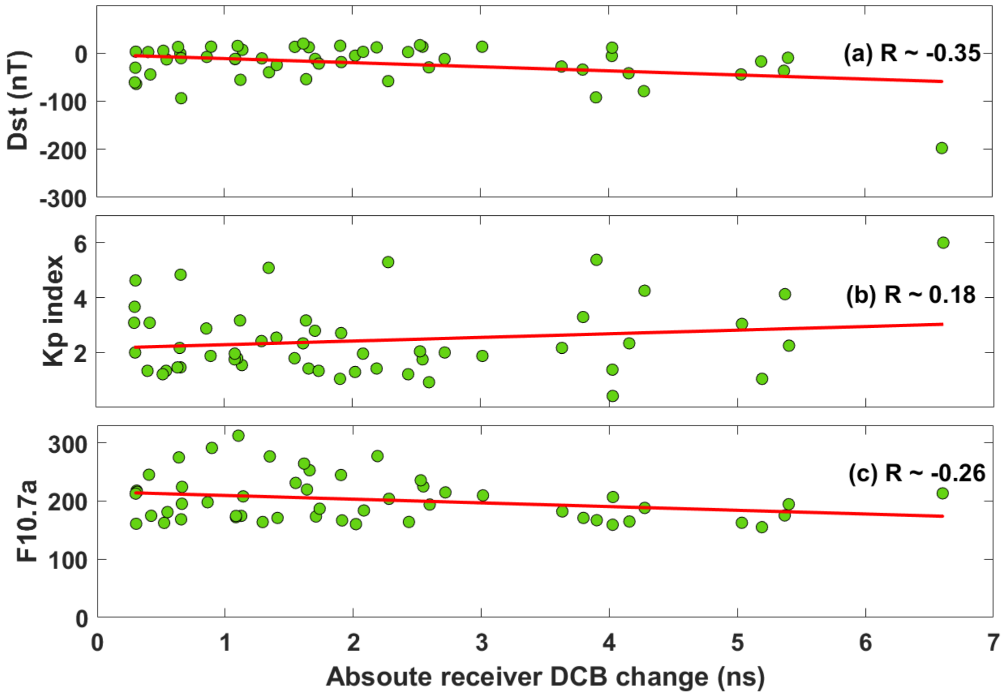

Figure 10. Correlations between the absolute receiver DCB change and three indices. (a) daily mean Dst value and absolute receiver DCB change, (b) daily mean Kp index and absolute receiver DCB change, and (c) F10.7a and the absolute receiver DCB change. The red solid lines are fitted by a linear regression model that minimizes the sum of the squared residuals.

A Pearson correlation was used to investigate the relationship between the two variables. The corresponding Pearson correlation coefficient (R) was calculated as a measure of the linear relationship. The R values between the receiver DCB change and the Dst, Kp, and F10.7a indices were –0.35, 0.18, and –0.26, respectively. The strong negative values of the Dst index during geomagnetic storms, as depicted in Figure 9a, suggest that the observed negative correlation may reflect the influence of geomagnetic disturbances on receiver DCB variability. Therefore, this indicates that a positive correlation exists between the two variables.

Figure 10b shows a weak positive correlation (R ~ 0.18) between the Kp index and the receiver DCB change. This implies that the correlation between the two variables is relatively weak.

As shown in Figure 10c, the F10.7a exhibited a moderate negative correlation (R ~ –0.26) with the receiver DCB change. This indicates that higher solar activity may correspond to somewhat smaller variations in the receiver DCB.

Our results suggest that the absolute changes in receiver DCBs are more strongly influenced by the Dst than the Kp and F10.7a.

Previous studies have reported that ionospheric conditions influence receiver DCB values [32,53,54]. In this study, we also investigated the correlation between receiver DCB variations and ionospheric VTEC values derived from shipborne GNSS observations. Figure 11 shows the correlation between the absolute change in receiver DCB and VTEC values. They revealed a weak positive correlation with an R of approximately 0.33.

Preprints.org (www.preprints.org) | NOT PEER-REVIEWED | Posted: 25 February 2026 doi:10.20944/preprints202602.1581.v1

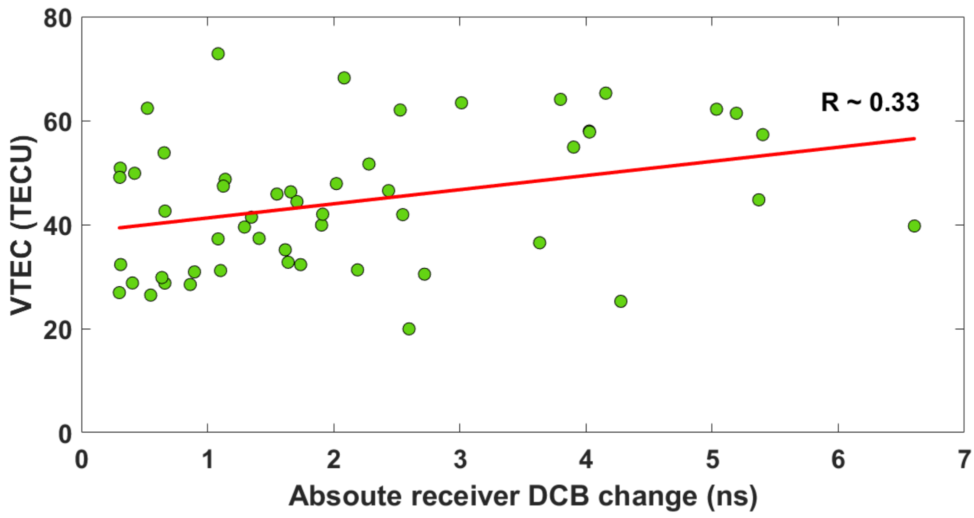

Figure 11. Correlation between the absolute receiver DCB change and VTEC. The red solid lines are fitted by a linear regression model that minimizes the sum of the squared residuals.

Figure 12 shows the multipath errors observed on the HANS. In most cases, the multipath-induced errors remained within 20 meters. However, in some cases, severe multipath effects were observed with errors exceeding 40 meters. Since large multipath errors may potentially affect the receiver DCB value, we analyzed the correlation between the two variables. In preparation for the correlation analysis, the multipath errors were converted with daily average value.

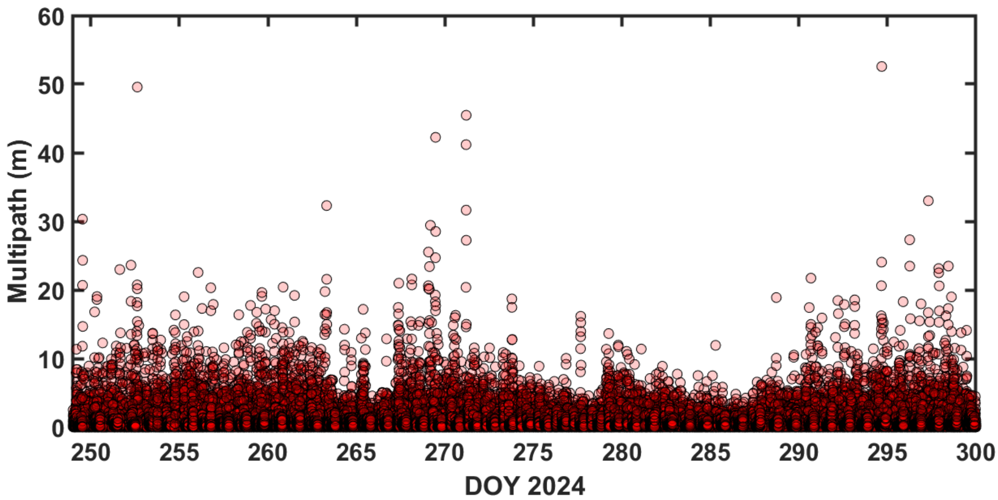

Figure 12. The time series of multipath error on the HANS ship from DOY 249 to 300, 2024. The red dots represent the multipath errors on the GPS L1 signal.

Figure 13 shows the correlation between the absolute receiver DCB changes and the daily mean multipath values. The result reveals that multipath errors exhibited a negligible correlation with receiver DCB change, as indicated by the **R** of 0.05. Significant multipath errors can undoubtedly be attributed to changes in the receiver's DCB. However, daily averaging these errors for correlation may have diminished their apparent impact.

Therefore, the significant variability in the receiver DCB observed on the HANS can be attributed to the complex interaction of several factors, including space weather conditions, geomagnetic activity, ionospheric TEC variability, and the ship's continuous motion.

Nevertheless, our results suggest that the HANS-derived receiver DCB exhibits a stronger correlation with Dst and VTEC.

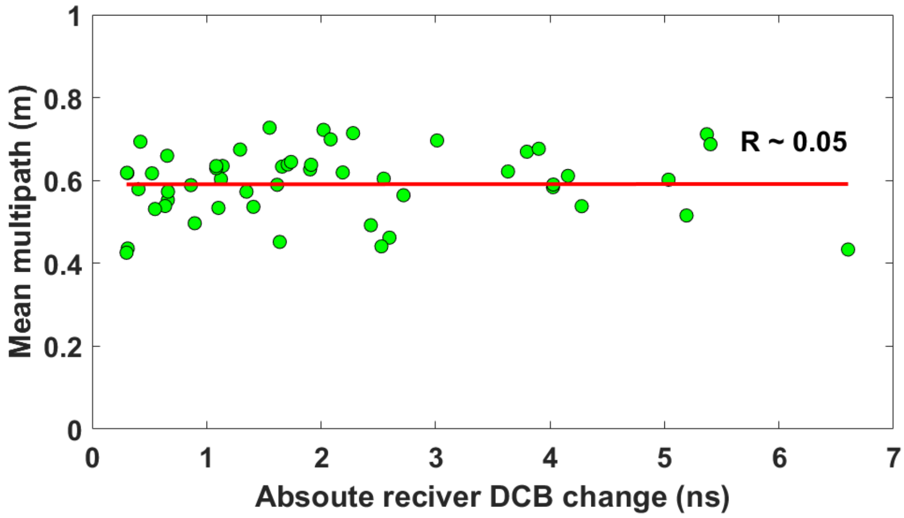

Figure 13. Correlation between the absolute receiver DCB change and multipath. The red solid lines are fitted by a linear regression model that minimizes the sum of the squared residuals.

6. Conclusions

This study estimated ionospheric TEC based on GPS/Galileo measurements recorded aboard the HANS ship from DOY 249 to 300 in 2024. Compared to the CODE GIM TEC, the TEC estimated from the HANS ship data showed a mean difference of –2.41 TECU and an RMS value of 6.53 TECU. The TEC values obtained from the HANS ship were found to be either overestimated or underestimated on some days relative to the CODE GIM TEC. Even with the incorporation of inland stations in South Korea aimed at stabilizing the DCB estimation for the HANS ship, the receiver DCB exhibited considerable variability.

Furthermore, we considered various factors that could potentially influence the receiver DCB value. As a preliminary step, correlations between receiver DCB changes and the Kp, Dst, and F10.7a indices were investigated. The negative correlation with the Dst index (R ~ –0.35) implies that geomagnetic disturbances contribute to increased fluctuations in the receiver DCB. While the correlations with the Kp (R ~ 0.18) and F10.7a (R ~ –0.26) were relatively low, these conditions can affect the stability of receiver DCB estimates. In addition, a positive correlation (R ~ 0.33) between receiver DCB changes and VTEC indicates that ionospheric TEC contributes to DCB variability.

Multipath errors on the HANS ship were occasional peaks over 40 meters. Although multipath effects have the potential to influence receiver DCB changes, the observed correlation between the two variables was very weak. This negligible correlation (R ~ 0.05) suggests that the daily average values may have mitigated the impact of short-term multipath fluctuations.

In conclusion, this study suggests the DCB values derived from shipborne GPS/Galileo observations have a strong correlation with Dst and VTEC. It can also be attributed to the interaction of several factors, such as space weather conditions, geomagnetic activity, ionospheric TEC variability, and the ship's continuous movements.

Author Contributions: Conceptualization, B.-K.C. and D.-H.S.; software, B.-K.C.; validation, B.-K.C. and D.-H.S.; formal analysis, B.-K.C. and D.-H.S..; investigation, B.-K.C. and D.-H.S.; data curation, D.-H.S., J.-K.C. and

 doi:10.20944/preprints202602.1581.v1

D.-J.H.; writing—original draft preparation, B.-K.C.; writing—review and editing, B.-K.C., D.-H.S., J.-K.C. and D.-J.H.; visualization, B.-K.C. All authors have read and agreed to the published version of the manuscript.

Funding: This study was supported by the Korea Astronomy and Space Science Institute under the R&D program (Project No. 2025-1-850-04) supervised by the Korea AeroSpace Administration.

Data Availability Statement: The RINEX files for processing can be downloaded from the GNSS integrated data center (https://www.gnssdata.or.kr/download/getDownloadView.do). The CODE GIMs are available through the NASA CDDIS archive (ftp://cddisa.gsfc.nasa.gov/pub/gps/products/ionex/, accessed on 1 August 2023).

Acknowledgments: We would like to thank the IGS and CODE for providing the GIM products. We are also deeply grateful to the Republic of Korea Navy for their cooperation and assistance with the maritime GNSS data collection.

Conflicts of Interest: The authors declare no conflicts of interest.

References

1. Schaer, S.; Beutler, G.; Rothacher, M. Mapping and Predicting the Ionosphere. In Proceedings of the IGS Analysis Center Workshop. Darmstadt, Germany, February 9-11, 1998; pp. 307-318.
2. Afraimovich, E.L.; Astafyeva, E.I.; Zhivetiev, I.V.; Oinats, A.V.; Yasyukevich, Y.V. Global Electron Content during Solar Cycle 23. *Geomagn. Aeron.* **2008**, *48*, 187-200. https://doi.org/10.1134/S0016793208020084
3. Mannucci, A.J.; Wilson, B.D.; Yuan, D.N.; Ho, C.H.; Lindqwister, U.J.; Runge, T.F. A global mapping technique for GPS-derived ionospheric total electron content measurements. *Radio Sci*. **1998**, *33*, 565-582. https://doi.org/10.1029/97RS02707
4. Juan, J.M.; Hernández-Pajares, M.; Sanz, J.; Ramos-Bosch, P.; Aragon-Angel, A.; Orus, R.; Ochieng, W.; Feng, S.; Jofre, M.; Coutinho, P.; et al. Enhanced Precise Point Positioning for GNSS Users. *IEEE Trans. Geosci. Remote Sens.* **2012**, *50*, 4213-4222.
5. Psychas, D.; Verhagen, S.; Liu, X.; Memarzadeh, Y.; Visser, H. Assessment of ionospheric corrections for PPP-RTK using regional ionosphere modelling. *Meas. Sci. Technol.* **2019**, *30*, 014001. https://doi.org/10.1088/1361-6501/aaefe5
6. Li, X.; Zhang, X.; Ge, M. Regional reference network augmented precise point positioning for instantaneous ambiguity resolution. *J. Geod.* **2011**, *85*, 151–158. https://doi.org/10.1007/s00190-010-0424-0
7. Hernández-Pajares, M.; Juan, J.M.; Sanz, J.; Orus, R.; Garcia-Rigo, A.; Feltens, J.; Komjathy, A.; Schaer, S.C.; Krankowski, A. The IGS VTEC maps: a reliable source of ionospheric information since 1998. *J. Geod.* **2009**, *83*, 263-275. https://doi.org/10.1007/s00190-008-0266-1
8. Wang, J.; Liu, Y.; Zhang, H.; Li, X. Estimation of Precipitable Water Vapor from Shipborne GNSS Observations over the Western Pacific Ocean. *Journal of Atmospheric and Oceanic Technology* **2020**, *37*, 657-670. https://doi.org/10.1175/JTECH-D-19-0140.1
9. Shoji, Y.; Tsuda, T.; Miyahara, S. Shipborne GNSS-Derived Precipitable Water Vapor Observations during Typhoon Passage over the Western North Pacific. *Atmospheric Measurement Techniques* **2017**, *10*, 3611-3623. https://doi.org/10.5194/amt-10-3611-2017
10. Li, Z.; Wang, J.; Hajj, G.A. Observations and modeling of the tropospheric delay using shipborne GPS. *Geophysical Research Letters* **2002**, *29*, 1595. https://doi.org/10.1029/2001GL013949
11. Sohn, D.-H.; Choi, B.-K.; Park, Y.; Kim, Y.C.; Ku, B. Precipitable Water Vapor Retrieval from Shipborne GNSS Observations on the Korean Research Vessel ISABU. *Sensors* **2020**, *20*, 4261. https://doi.org/10.3390/s20154261
12. Mannucci, A.; Iijima, B.; Lindqwister, U.; Pi, X.; Sparks, L.; Wilson, B. *GPS and Ionosphere: Review of Radio Science 1996-1999*; Oxford Univ. Press: New York, NY, USA, 1999
13. Hernández-Pajares, M. *Performance of IGS Ionosphere TEC Maps*; Technical University of Catalonia: Barcelona, Spain, 2003
14. Hernández-Pajares, M. *IGS Ionosphere WG Status Report: Performance of IGS Ionosphere TEC Maps*; IGS Workshop: Bern, Switzerland, 2004

15. Luo, X.; Xu, H.; Li, Z.; Zhang, T.; Gao, J.; Shen, Z.; Yang, C.; Wu, Z. Accuracy assessment of the global ionospheric model over the Southern Ocean based on dynamic observation. *J. Atmos. Sol. Terr. Phys.* **2017**, *154*, 127-131. https://doi.org/10.1016/j.jastp.2016.12.017
16. Luo, X.; Wang, D.; Wang, J.; Wu, Z.; Gao, J.; Zhang, T.; Yang, C.; Qin, X.; Chen, X. Study of the Spatiotemporal Characteristics of the Equatorial Ionization Anomaly Using Shipborne Multi-GNSS Data: A Case Analysis (120–150°E, Western Pacific Ocean, 2014–2015). *Remote Sens.* **2021**, *13*, 3051. https://doi.org/10.3390/rs13153051
17. Wang, D.; Luo, X.; Wang, J.; Gao, J.; Zhang, T.; Wu, Z.; Yang, C.; Wu, Z. Global Ionospheric Model Accuracy Analysis Using Shipborne Kinematic GPS Data in the Arctic Circle. *Remote Sens.* **2019**, *11*, 2062. https://doi.org/10.3390/rs11172062
18. Azeem, I.; Vadas, S.L.; Crowley, G.; Makela, J.J. Traveling ionospheric disturbances over the United States induced by gravity waves from the 2011 Tohoku tsunami and comparison with gravity wave dissipative theory. *Journal of Geophysical Research: Space Physics* **2017**, 122, 3430-3447. https://doi.org/10.1002/2016JA023659
19. Codrescu, M.V.; Palo, S.E.; Zhang, X.; Fuller-Rowell, T.J., Poppe, C. TEC climatology derived from TOPEX/Poseidon measurements. *Journal of Atmospheric and Solar Terrestrial Physics* **1999**, *61*, 281-298. https://doi.org/10.1016/S1364-6826(98)00132-1
20. Lei, J.; Syndergaard, S.; Burns, A.G.; Solomon, S.C.; Wang, W.; Zeng, Z.; Roble, R.G.; Wu, Q.; Kuo, Y.H.; Holt, J.M.; Zhang, S.R.; Hysell, D.L.; Rodrigues, F.S.; Lin, C.H. Comparison of COSMIC ionospheric measurements with ground-based observations and model predictions: Preliminary results. *Journal of Geophysical Research* **2007**, *112*, A07308. https://doi.org/10.1029/2006JA012240
21. Schreiner, W.; Rocken, C.; Sokolovskiy, S.; Syndergaard, S.; Hunt, D. Estimates of the precision of GPS radio occultations from the COSMIC/FORMOSAT-3 mission. *Geophysical Research Letters* **2007**, *34*, L04808. https://doi.org/10.1029/2006GL027557
22. Schreiner, W.S.; Weiss, J.P.; Anthes, R.A.; Braun, J.; Chu, V.; Fong, J.; Hunt, D.; Kuo, Y.H.; Meehan, T.; Serafino, W.; Sjoberg, J.; Sokolovskiy, S.; Talaat, E.; Wee, T.K.; Zeng, Z. COSMIC-2 radio occultation constellation: First results. *Geophysical Research Letters* **2020**, *47*, e2019GL086841. https://doi.org/10.1029/2019GL086841
23. Ma, X.F.; Maruyama, T.; Ma, G.; Takeda, T. Determination of GPS receiver differential biases by neural network parameter estimation method, *Radio Sci*. **2005**, *40*, RS1002, doi:10.1029/2004RS003072.
24. Choi, B.-K.; Park, J.U.; Roh, K.M.; Lee, S.J. Comparison of GPS receiver DCB estimation methods using a GPS network. *Earth Planet Space* **2013**, *65*, 707-711. https://doi.org/10.5047/eps.2012.10.003
25. Montenbruck, O.; Hauschild, A.; Steigenberger, P. Differential Code Bias Estimation using Multi-GNSS Observations and Global Ionosphere Maps, *Navigation* **2014**, *61*, 191-201. https://doi.org/10.1002/navi.64
26. Xue, J.; Song, S., Liao, X., Zhu, W. Estimating and assessing Galileo navigation system satellite and receiver differential code biases using the ionospheric parameter and differential code bias joint estimation approach with multi-GNSS observations, *Radio Sci*. **2016**, *51*, 271-283. https://doi.org/10.1002/2015RS005797
27. Ma, G.; Maruyama, T. Derivation of TEC and estimation of instrumental biases from GEONET in Japan. *Ann. Geophys*. **2003**, *21*, 2083-2093. https://doi.org/10.5194/angeo-21-2083-2003
28. Sardón, E.; Rius, A.; Zarraoa, N. Estimation of the transmitter and receiver differential biases and the ionospheric total electron content from global positioning system observations, *Radio Sci.* **1994**, *29*, 577–586. https://doi.org/10.1029/94RS00449
29. Wang, Q.; Jin, S.; Hu, Y. Estimation of QZSS differential code biases using QZSS/GPS combined observations from MGEX, *Adv. Space Res*. **2021**, *67*, 1049-1057. https://doi.org/10.1016/j.asr.2020.10.049
30. Wang, Y.; Li, M.; Yuan, Y.; Wen, G.; Zhou, F.; Geng, H. Analysis of factors affecting the estimation of the multi-GNSS satellite differential code biases (SDCBs). *Adv. Space Res*. **2024**, *74*, 65-74. https://doi.org/10.1016/j.asr.2024.03.041
31. Lanyi, G. E.; Roth, T. A comparison of mapped and measured total ionospheric electron content using global positioning system and beacon satellite observations. *Radio Sci.* **1988**, *23*, 483-492. https://doi.org/10.1029/RS023i004p00483

32. Zhang, D.H.; Zhang, W.; Li, Q.; Shi, L.Q; Xiao, Z. Accuracy Analysis of the GPS Instrumental Bias Estimated from Observations in Middle and Low Latitudes. *Ann. Geophys*. **2010**, *28*, 1571-1580. https://doi.org/10.5194/angeo-28-1571-2010
33. Coco, D.S.; Coker, C.; Dahlke, S.R.; Clynch, J.R. Variability of GPS satellite differential group delay biases, *IEEE Trans. Aerosp. Electron. Syst.* **1991**, *27*, 931–938. https://doi.org/10.1109/7.104264
34. Jakowski, N.; Schlüter, S.; Sardon, E. Total electron content of the ionosphere during the geomagnetic storm on 10 January 1997. *J. Atmos. Sol.-Terr. Phys*. **1999**, *61*, 299-307. https://doi.org/10.1016/S1364-6826(98)00130-8
35. Zhang, R.; Song, W.; Yao, Y.; Shi, C.; Lou, Y., Yi, W. Modeling regional ionospheric delay with ground-based BeiDou and GPS observations in China. *GPS Solut*. **2014**, *19*, 649-658. https://doi. org/10.1007/s10291-014-0419-z
36. Sardon, E.; Zarraoa, N. Estimation of the total electron content using GPS data: How stable are the differential satellite and receiver instrumental biases?. *Radio Sci*. **1997**, *32*, 1899-1910. https://doi.org/10.1029/97RS01457
37. Rama Rao, P.V.S.; Gopi Krishna, S.; Niranjan, K.; Prasad, D.S.V.V.D. Temporal and spatial variations in TEC using simultaneous measurements from the Indian GPS network of receivers during the low solar activity period of 2004–2005. *Ann. Geophys*. **2006**, *24*, 3279–3292. https://doi.org/10.5194/angeo-24-3279-2006
38. Klobuchar, J.A. Design and characteristics of the GPS ionospheric time-delay algorithm for single-frequency users. In Proceedings of the PLANS '86 Position Location and Navigation Symposium. Las Vegas, NV, USA, November 4-7, **1986**, pp. 280-286.
39. Klobuchar, J.A. Ionospheric time-delay algorithm for single-frequency GPS users. *IEEE Trans. Aerosp. Electron. Syst*. **1987**, *3*, 325-331. https://doi.org/10.1109/TAES.1987.310829
40. Yuan, Y.; Wang, N.; Li, Z.; Huo, X. The BeiDou Global Broadcast Ionospheric Delay Correction Model (BDGIM) and Its Preliminary Performance Evaluation Results. *Navigation* **2019**, *66*, 55-69. https://doi.org/10.1002/navi.292
41. Otsuka, Y.; Ogawa, T.; Saito, A.; Tsugawa, T.; Fukao, S.; Miyazaki, S. A new technique for mapping of total electron content using GPS network in Japan. *Earth Planets Space* **2002**. *54*, 63-70. https://doi.org/10.1186/BF03352422
42. Yang, Y.; Xu, Y.; Li, J.; Yang, C. Progress and performance evaluation of BeiDou global navigation satellite system: data analysis based on BDS-3 demonstration system. *Sci. China Earth Sci*. **2018**, *61*, 614– 624. https://doi.org/10.1007/s11430-017-9186-9
43. Wang, Q.; Jin, S.; Hu, Y. Estimation of QZSS differential code biases using QZSS/GPS combined observations from MGEX. *Adv. Space Res*. **2021**, *67*, 1049-1057. https://doi.org/10.1016/j.asr.2020.10.049
44. Schaer, S.; Beutler, G.; Mervart, L.; Rothacher, M.; Wild, U. Global and regional ionosphere models using the GPS double difference phase observable. In Proceedings of the IGS Workshop **1995**, GFZ, Potsdam, Germany, 15-18 May 1995; pp. 77-92.
45. Wang, Y.; Yue, D.; Wang, H.; Ma, H.; Liu, Z.; Yue, C. Comprehensive Analysis of BDS/GNSS Differential Code Bias and Compatibility Performance. *Remote Sens.* **2024**, *16*, 4217. https://doi.org/10.3390/rs16224217
46. Pi, X.; Mannucci, A.J.; Lindqwister, U.J.; Ho C.M. Monitoring of global ionospheric irregularities using the worldwide GPS network. *Geophys. Res. Lett.* **1997**, *24*, 2283-2286. https://doi.org/10.1029/97GL02273
47. Yao, Y.; Liu, L.; Kong, J.; Zhai, C. Analysis of the global ionospheric disturbances of the March 2015 great storm. *J. Geophys. Res. Space Physics* **2016**, *121*, 12, 157-12,170. https://doi.org/10.1002/2016JA02335
48. Zhang, D.; Shi, H.; Jin, Y.; Zhang, W.; Hao, Y.; Xiao, Z. The variation of the estimated GPS instrumental bias and its possible connection with ionospheric variability. *Sci. China Technol. Sci.* **2014**, *57*, 67–79. https://doi.org/10.1007/s11431-013-5419-7
49. Warnant, R. Reliability of the TEC computed using GPS measurements - The problem of hardware biases. *Acta. Geod. Geophys. Hung*. **1997**, 32, 451–459. https://doi.org/10.1007/BF03325514
50. Coster, A.; Williams, J.; Weatherwax, A.; Rideout, W.; Herne, D. Accuracy of GPS total electron content: GPS receiver bias temperature dependence. *Radio Sci.* **2013**, *48*, 190-196. https://doi.org/10.1002/rds.20011

 doi:10.20944/preprints202602.1581.v1

51. Yasyukevich, Y.V.; Mylnikova, A.A.; Kunitsyn, V.E.; Padokhin, A.M. Influence of GPS/GLONASS differential code biases on the determination accuracy of the absolute total electron content in the ionosphere. *Geomag. Aeronomy* **2015**, *55*, 763-769. https://doi.org/10.1134/S001679321506016
52. Choi, B.-K.; Lee, S.J. The influence of grounding on GPS receiver differential code biases. *Adv. Space Res*. **2018**, *62*, 457-463. https://doi.org/10.1016/j.asr.2018.04.033
53. Zhang, X.; Xia, L.; Lin, H.; Li, Q. Epoch-Wise Estimation and Analysis of GNSS Receiver DCB under High and Low Solar Activity Conditions. *Remote Sens.* **2023**, *15*, 2190. https://doi.org/10.3390/rs15082190
54. Choi, B.-K.; Sohn, D.-H.; Lee, S.J. Correlation between Ionospheric TEC and the DCB Stability of GNSS Receiver from 2014 to 2016. *Remote Sens.* **2019**, *11*, 2657, doi:10.3390/RS11222657